ACS APPLIED MATERIALS & INTERFACES

www.acsami.org

Research Article

Substrate Modification during Chemical Vapor Deposition of hBN on Sapphire

Anushka Bansal, Maria Hilse, Benjamin Huet, Ke Wang, Azimkhan Kozhakhmetov, Ji Hyun Kim, Saiphaneendra Bachu, Nasim Alem, Ramon Collazo, Joshua A. Robinson, Roman Engel-Herbert, and Joan M. Redwing*

Cite This: *ACS Appl. Mater. Interfaces* 2021, 13, 54516−54526

Read Online

ACCESS | Metrics & More | Article Recommendations | Supporting Information

ABSTRACT: A comparison of hexagonal boron nitride (hBN) layers grown by chemical vapor deposition on *C*-plane (0001) versus *A*-plane ($11\bar{2}0$) sapphire (α-Al_2O_3) substrate is reported. The high deposition temperature (>1200 °C) and hydrogen ambient used for hBN deposition on sapphire substantially alters the *C*-plane sapphire surface chemistry and leaves the top layer(s) oxygen deficient. The resulting surface morphology due to H_2 etching of *C*-plane sapphire is inhomogeneous with increased surface roughness which causes non-uniform residual stress in the deposited hBN film. In contrast to *C*-plane, the *A*-plane of sapphire does not alter substantially under a similar high temperature H_2 environment, thus providing a more stable alternative substrate for high quality hBN growth. The E_{2g} Raman mode full width at half-maximum (FWHM) for hBN deposited on *C*-plane sapphire is 24.5 ± 2.1 cm^{-1} while for hBN on *A*-plane sapphire is 24.5 ± 0.7 cm^{-1}. The lesser FWHM standard deviation on *A*-plane sapphire indicates uniform stress distribution across the film due to reduced undulations on the surface. The photoluminescence spectra of the hBN films at 300 and 3 K, obtained on *C*-plane and *A*-plane sapphire exhibit similar characteristics with peaks at 4.1 and 5.3 eV reported to be signature peaks associated with defects for hBN films deposited under lower V/III ratios. The dielectric breakdown field of hBN deposited on *A*-plane sapphire was measured to be 5 MV cm^{-1}, agreeing well with reports on mechanically exfoliated hBN flakes. Thus, under the typical growth conditions required for high crystalline quality hBN growth, *A*-plane sapphire provides a more chemically stable substrate.

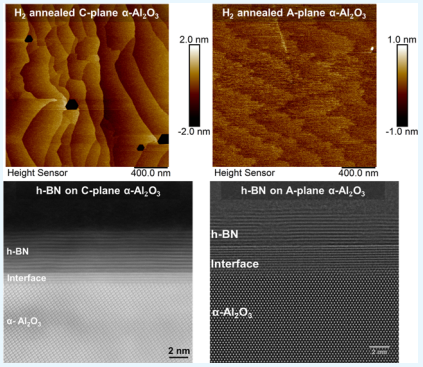

KEYWORDS: *chemical vapor deposition, hexagonal boron nitride, 2D material, III−V nitrides, surface reconstruction, RHEED, dielectric breakdown*

1. INTRODUCTION

Since the advent of graphene in 2004, the field of atomically thin two-dimensional (2D) materials has expanded exponentially. Hexagonal boron nitride (hBN), belonging to the family of 2D materials, is a group III-nitride wide bandgap semiconductor that has a layered crystal structure similar to graphite, with B and N atoms covalently bonded in a hexagonal lattice within the layer and van der Waals (vdW) bonding between layers. Due to its extraordinary physical properties, such as high resistivity, high thermal conductivity, high dielectric breakdown field, stability in air up to 1000 °C and large bandgap (E_g ~ 5.9 eV), hBN appears to be a promising material for emerging applications, including deep ultraviolet optoelectronics, single photon emitters (SPEs), neutron detectors and so forth.[1−10] There is also significant interest in monolayer and few-layer hBN as an encapsulating/dielectric layer for 2D devices based on graphene and transition metal dichalcogenides.[11,12] While high quality hBN bulk crystals are available for exfoliation, the size of the crystals is limited, consequently there is continued interest in the epitaxial growth of large area hBN films using chemical vapor deposition (CVD) for use in practical applications.

Thin film hBN deposition on metallic substrates such as Cu, Ni, Pt, Ru at typical growth temperatures of <1100 °C has been widely studied.[13−16] However, for many electronics and opto-electronics applications, there is an interest in transfer-free deposition of hBN on insulating/transparent substrates like sapphire (Al_2O_3). The growth of thin sp^2-BN films on Al_2O_3 substrate was initially reported by Nakamura in 1986, which suggested that to deposit sp^2-BN with a *c*-axis lattice constant similar to that of bulk hBN, a growth temperature of 1500 °C was necessary.[17] It was experimentally validated by Kobayashi et al. in 2008, followed by others, that growth

Received: August 4, 2021
Accepted: October 26, 2021
Published: November 8, 2021

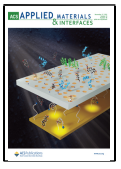

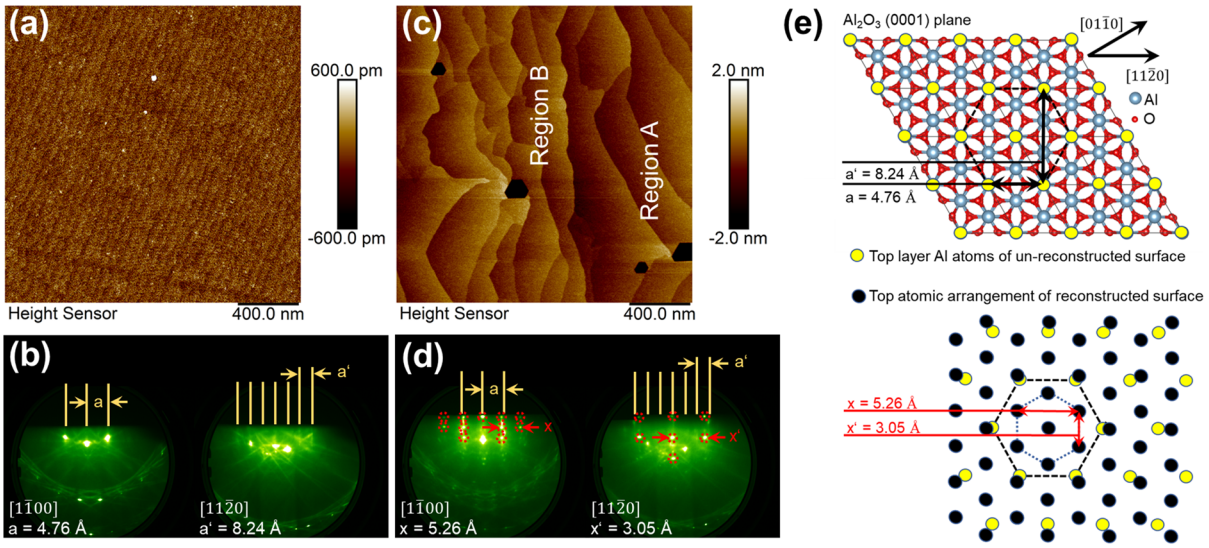

Figure 1. (a) AFM image of the as-received *C*-plane sapphire substrate (b) typical RHEED pattern obtained for un-reconstructed as-received sapphire substrate. Yellow lines indicate spacing between diffraction streaks in the [1$\bar{1}$00] and [11$\bar{2}$0] azimuth represented by *a* and *a*′ respectively. (c) AFM image of the H_2 annealed sapphire surface at 1300 °C with hexagonal pits and modified steps; two regions marked A and B are representative of two different step sizes and terrace widths observed across the annealed substrate (d) RHEED pattern obtained for H_2 annealed *C*-plane sapphire substrate. Yellow lines indicate spacing between diffraction streaks in the [1$\bar{1}$00] and [11$\bar{2}$0] azimuth represented by *a* and *a*′ respectively. The red circles indicate spacing between diffraction spots by *x* and *x*′ respectively along different azimuth directions. These diffraction spots originate from the reconstructions happening at the substrate surface. (e) Top image showing surface Al atoms (yellow color) on the un-reconstructed *C*-plane sapphire surface with *a* and *a*′ marked. Bottom image shows modified arrangement of Al atoms on the H_2 annealed surface as observed using RHEED. The black circles connected by blue dashed lines represent 30° rotation of Al atoms compared to the bulk of the substrate and the dimensions of *x* and *x*′.

temperatures greater than 1200 °C are sufficient to obtain hBN which otherwise leads to a turbostratic form of BN at lower temperatures.[18−21] The typical precursors used for hBN growth on non-metallic substrates include triethyl boron [$B(C_2H_5)_3$, TEB], trimethyl boron [$B(CH_3)_3$, TMB] for B and ammonia (NH_3) as the source of N. It is well known, however, that organic sources such as TEB can result in carbon incorporation in the film which is a concern for the growth of high purity hBN films[22,23] Moreover, for applications such as quantum computing and sensing that utilize SPE centers in hBN, excessive carbon contamination in the film could be an issue due to high autofluorescence, thus making it challenging to isolate individual structural defects in hBN, limiting the use of hBN for such applications.[24,25] Therefore, using carbon free hydride precursors such as diborane (B_2H_6) and NH_3 for B and N respectively, one can potentially eliminate the issue with C contamination in the films.

However, as mentioned earlier, high quality hBN film deposition requires high growth temperatures (>1200 °C). Thus, it becomes extremely important to investigate the stability of widely used crystalline substrates such as Al_2O_3 in this temperature range. Prior studies have investigated pre-treatment of the sapphire substrate with NH_3 to form a thin AlN buffer layer prior to growth of hBN which results in a high crystalline quality hBN on sapphire substrate.[20,26] While the formation of AlN may serve to stabilize the substrate surface at high temperatures in H_2, the effect of H_2 in the absence of a nitride surface has not yet been examined yet. It was reported that graphene nucleation and growth on sapphire at ∼1150−1250 °C is self-catalytic, given that oxygen (O) etches away from the surface of Al_2O_3 forming Al-rich pits in the case of *A*-plane and *C*-plane Al_2O_3 which serve as nucleation points for graphene growth.[27] Recently, Mishra et al. identified the Al-rich $\sqrt{31} \times \sqrt{31} \pm 9°$reconstruction of Al_2O_3 to be crucial for obtaining epitaxial CVD graphene on *C*-plane Al_2O_3.[27−29] Similarly, for the case of hBN grown by MBE at a substrate temperature of ∼1250 °C, it has been reported that the sapphire surface reconstructs into $\sqrt{31} \times \sqrt{31} \pm 9°$ under ultra-high vacuum conditions.[30] In the case of CVD of hBN at high growth temperatures (>1200 °C), the presence of hydrogen in the growth ambient is expected to also modify the sapphire surface but this has not yet been investigated in detail.

In this study, the impact of a H_2 environment at high deposition temperature (1300 °C) on the α-Al_2O_3 surface was investigated for two crystallographic orientations (*C*-plane (0001) and *A*-plane (11$\bar{2}$0) Al_2O_3). hBN films grown on *C*-plane and *A*-plane sapphire exhibited similar structural and optical properties as assessed by Raman spectroscopy, transmission electron microscope (TEM) and low temperature photoluminescence (PL) measurements. However, the *C*-plane sapphire surface was found to undergo significant etching in H_2 at high temperature which results in inhomogeneous stress in the hBN film after deposition. In contrast, the *A*-plane surface exhibited significantly better stability at these growth conditions resulting in a more uniform hBN film. The results are explained in terms of the differences in interplanar spacing of the two crystallographic orientations which impacts their thermal stability.

2. RESULTS AND DISCUSSION

The surface of the *C*-plane α-Al_2O_3 (0001) substrates, as-received and after annealing at 1300 °C in H_2 was initially examined. As-received nominally on-axis *C*-plane sapphire substrates exhibit an average surface roughness of 0.2 nm and consist of parallel steps oriented toward the [10$\bar{1}$0] direction

https://doi.org/10.1021/acsami.1c14591
ACS Appl. Mater. Interfaces 2021, 13, 54516−54526

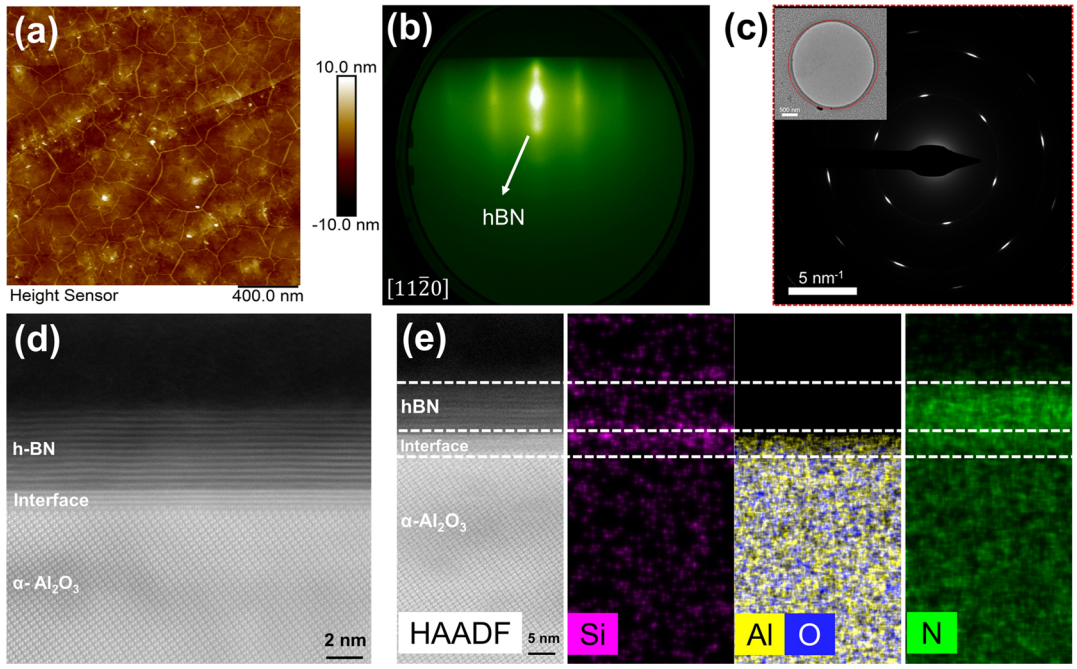

Figure 2. (a) AFM image of hBN deposited on *C*-plane sapphire. (b) RHEED pattern of the obtained hBN film along the [11$\bar{2}$0] azimuth indicating 30° misorientation between the substrate and the film. (c) SAED pattern showing oriented hBN films with some degree of polycrystallinity as indicated by faint rings between the bright spots collected from the circled the area in the inset. The inset is a low magnification plan view TEM image showing a continuous film of hBN transferred on a TEM grid. (d) Cross-section high-angle annular dark field scanning transmission electron microscopy (HAADF-STEM) image of ∼3 nm BN grown on sapphire along zone axis [11$\bar{2}$0] showing a crystalline interface between hBN and sapphire. (e) HAADF image and corresponding EDS elemental maps of Si, Al, O and N respectively indicating an interface composed of Al, O, Si and N.

with an average step height of 0.1 nm and average terrace width of ∼60 nm as shown in the atomic force microscopy (AFM) image in Figure 1a. Figure 1b displays the reflection high energy electron diffraction (RHEED) images observed for the as-received *C*-plane sapphire substrate along the ⟨1$\bar{1}$00⟩ and ⟨11$\bar{2}$0⟩ azimuths. The surface exhibits an un-reconstructed pattern with lattice diffraction streaks with a spacing of a = 4.76 Å in the ⟨1$\bar{1}$00⟩ azimuth, corresponding to a lattice constant of bulk sapphire and a spacing of 8.24 Å in the ⟨11$\bar{2}$0⟩ azimuth corresponding to $a' = \sqrt{3} \times a$ (highlighted by yellow lines). After H_2 annealing at 1300 °C for 10 min, prior to hBN deposition, the sapphire surface is altered considerably as shown in the AFM image in Figure 1c. The average surface roughness increases to 0.5 nm and hexagonal-shaped pits appear on the surface. Also, H_2 annealing causes the terrace width to change with regions of wider terraces (region A) with an average terrace width of ∼340 nm and an average step height of 0.65 nm and narrow terraces (region B) with an average terrace width of 190 nm and an average step height of 0.40 nm. In the RHEED pattern (Figure 1d) taken along the ⟨1$\bar{1}$00⟩ and ⟨11$\bar{2}$0⟩ azimuths post H_2 annealing, the diffraction spots from un-reconstructed sapphire indicated by yellow lines are still present, however, they consist of spots as compared to streaky features observed before annealing (Figure 1d). Such transitions from streaks to spots in RHEED diffraction patterns reflect increased surface roughness, which is consistent with the topographical analysis by AFM (Figure 1a,c). Besides the diffraction spots from the un-reconstructed sapphire surface, a second distinct diffraction pattern of rectangular symmetry with a different lattice spacing in both azimuths is apparent in Figure 1d, indicated with red dashed circles. The derived lattice spacings x and x' of the secondary pattern amount to 5.26 and 3.05 Å in the ⟨1$\bar{1}$00⟩ and ⟨11$\bar{2}$0⟩ azimuths, respectively, revealing the relationship $x = \sqrt{3} \times x'$ of a hexagonal atomic arrangement of the surface atoms. This observed superstructure and its relationship to the un-reconstructed sapphire (0001) surface is sketched in Figure 1e. The top Al atoms of the un-reconstructed surface are represented by yellow circles, that arrange in a hexagonal in-plane symmetry demonstrated by the black dashed hexagon lattice cell with the given dimensions a and a'. This top layer of un-reconstructed Al atoms of the sapphire (0001) plane is overlayed by the secondary surface atom arrangement deduced from RHEED in black circles in the bottom part of Figure 1e for better visualization. Compared to the hexagonal in-plane lattice cell (hexagon in black dashed line) of the pristine *C*-plane α-Al_2O_3, the in-plane hexagonal superstructure lattice cell of H_2 annealed *C*-plane α-Al_2O_3 (hexagon in blue dashed line), is rotated by 30° and the dimension of x and x' make it about 64% smaller than the sapphire bulk atomic arrangement.

The reconstructions and surface rearrangements of *C*-plane α-Al_2O_3 has been a subject of study in the literature,[31−33] and it was found that annealing procedures at high temperatures in general and especially in the presence of H_2 drive out oxygen atoms from the bulk sapphire crystal and the surface terminates in an Al layer, which relaxes into a 50−88% smaller lattice than the bulk crystal.[31] In addition, traces of hydrogen atoms were found on those surfaces.[31] Thus, our observation of a crystal relaxation of about 64% is in agreement with these earlier reports. However, assuming the top superstructure consists of a pure Al layer, the strain in the layer would amount to about 6% for the fcc Al bulk crystal lattice with a = 4.05 Å, that is, an in-plane lattice constant of the (111) plane of 2.865 Å to match our RHEED observations. Even though hydrogen atoms were

https://doi.org/10.1021/acsami.1c14591
ACS Appl. Mater. Interfaces 2021, 13, 54516−54526

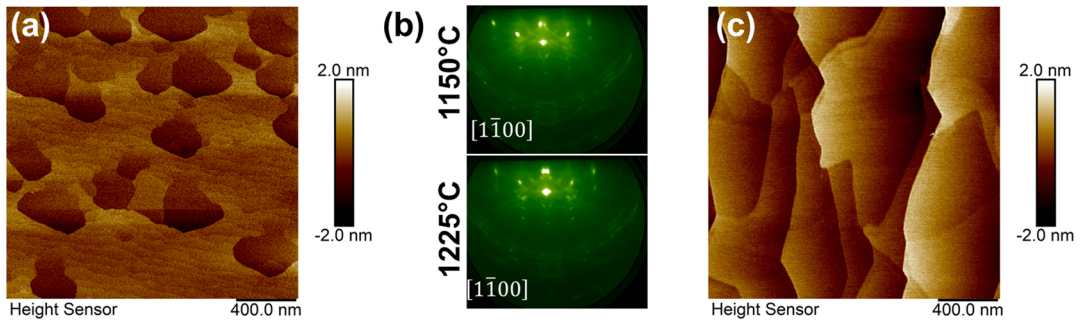

Figure 3. (a) AFM image of the H_2 annealed sapphire surface at 1150 °C where the surface starts to modify with visible shallow pits, however most of the surface still looks like the as-received sapphire substrate. (b) RHEED patterns of H_2 annealed sapphire substrates at 1150 and 1225 °C along [1$\bar{1}$00] azimuth. (c) AFM image of the H_2 annealed sapphire surface at 1225 °C showing major modification of the sapphire with wider terraces.

detected on the surface in earlier reports as well, the dimensions of the superstructure in this work do not agree with any of the reported AlH_3 phases.[34,35] It should also be noted that the RHEED patterns in Figure 1d shows a large amount of additional dense diffraction spots of low intensity scattered along semi-circles of different radius around the center of the RHEED horizon between the already discussed main more intense diffraction spots. Those indicate an atomic rearrangement of the outermost sapphire surface atoms, that is surface reconstruction in addition to the superimposed superstructure. A variety of complex surface reconstructions of the (0001) plane of sapphire are well-studied to date, such as the $(2\sqrt{3} \times 2\sqrt{3})R30°$, $(3\sqrt{3} \times 3\sqrt{3})R30°$, and $(\sqrt{31} \times \sqrt{31})R \pm 9°$.[31,33] However, it is difficult to assign a specific one to the pattern in Figure 1d because of the low intensity of the reconstruction diffraction spots. Moreover, the reconstruction observed in this work might not be among the pool of previously reported sapphire surface reconstructions due to a partial reversal of the high temperature reconstruction during the room temperature (RT) transfer from the CVD chamber to the MBE system or the high probability of hydrogen atoms present on the surface after the anneal in hydrogen gas. Overall, the data presented in Figure 1 demonstrates that the 10 min H_2 anneal at 1300 °C substantially alters the *C*-plane sapphire surface configuration and leaves the top layer(s) oxygen deficient, most likely Al rich, and probably terminated by hydrogen atoms.

Following H_2 annealing of *C*-plane α-Al_2O_3, hBN was deposited using the flow modulation epitaxy (FME) approach with 200 alternating pulses of B_2H_6 and NH_3. A continuous hBN film is obtained, exhibiting wrinkles due to differences in the coefficient of thermal expansion (CTE) mismatch between sapphire and hBN.[36] Using Fourier transform infrared (FTIR) spectroscopy, the film thickness is measured to be 3.2 nm (~11 layers) indicating a growth rate of ~19.2 nm/h. The average surface roughness measured is 0.9 nm with an average wrinkle height of 1.4 nm using AFM (Figure 2a). The RHEED pattern of the hBN film on sapphire suggests a rotationally oriented, crystalline hBN film with $[11\bar{2}0]_{hBN} \| [1\bar{1}00]_{sapphire}$ epitaxial relation (Figure 2b) similar to previous observations.[37,38] The 30° misorientation between the substrate and the film significantly reduces the lattice mismatch from 47.4% in the case of unrotated to 9%. Figure 2c inset shows a low magnification TEM image of the transferred hBN film on a TEM grid. The transferred film is continuous with minimal out of plane growth. The corresponding selected area electron diffraction (SAED) pattern (Figure 2c) shows the film is highly crystalline (six bright hexagonal spots) with some degree of polycrystallinity (faint ring connecting the bright spots). To directly observe the film thickness, hBN stacking sequence, and interface between hBN and sapphire, high-resolution cross-sectional scanning TEM (STEM) was performed along [11$\bar{2}$0] zone axis of the sapphire substrate. Figure 2d shows a high angle annular dark field (HAADF) STEM cross section of an hBN film deposited on *C*-plane sapphire, demonstrating the layered sp^2 nature of BN film. Due to slight misorientation between sp^2-BN and the substrate lattice, it was difficult to observe atomic columns of sp^2-BN to identify hexagonal (ABAB...) versus rhombohedral (ABCABC...) phase. Chubarov et al. performed a detailed study on identifying the stable phase of sp^2-BN films obtained on *C*-plane sapphire with an AlN buffer layer; they observed that growth initiates as hBN but after thickness of ~4 nm, transitions to rBN (rhombohedral).[19] In this case, since the film thickness is <4 nm, the sp^2 BN is expected to be hexagonal. A crystalline interface is observed between hBN and *C*-plane sapphire as marked in Figure 2d. To understand the composition of the interface, energy dispersive X-ray spectroscopy (EDS) mapping was performed. Figure 2e is a HAADF-STEM image of this sample and corresponding EDS maps. The interface is primarily composed of Al, O, N and Si. The unintentional Si is believed to arise from Si sublimation at 1300 °C from the SiC-coated graphite susceptor used to heat the sapphire substrate during CVD which can subsequently deposit on the sapphire surface and become incorporated at the film-substrate interface.

To measure the effect of the inhomogeneous surface topography of the *C*-plane sapphire substrate on the lateral distribution of residual stress in the hBN film, Raman mapping was performed to measure peak position and full width at half-maximum (fwhm) of the E_{2g} Raman active mode of hBN across an area of 5 μm × 5 μm (Figure S1a,b in the (Supporting Information). The average E_{2g} peak position is measured to be 1368.5 ± 0.7 cm^{-1} with a fwhm of 24.5 ± 2.1 cm^{-1} across a 25 μm^2 area. The peak position is higher in wavenumber than the reported value for stress-free hBN film/bulk hBN which has a peak position at 1365 cm^{-1}.[39,40] This indicates residual compressive stress in the films after cooling down to RT. The standard deviation in the average peak position and FWHM indicates inhomogeneous stress distribution across the film even though the film thickness is constant. This could be due to inhomogeneities on the substrate surface resulting in non-uniform residual stress in the film. The transfer of 2D materials from their growth substrate is well known to relax film stress resulting from the growth

https://doi.org/10.1021/acsami.1c14591
ACS Appl. Mater. Interfaces 2021, 13, 54516−54526

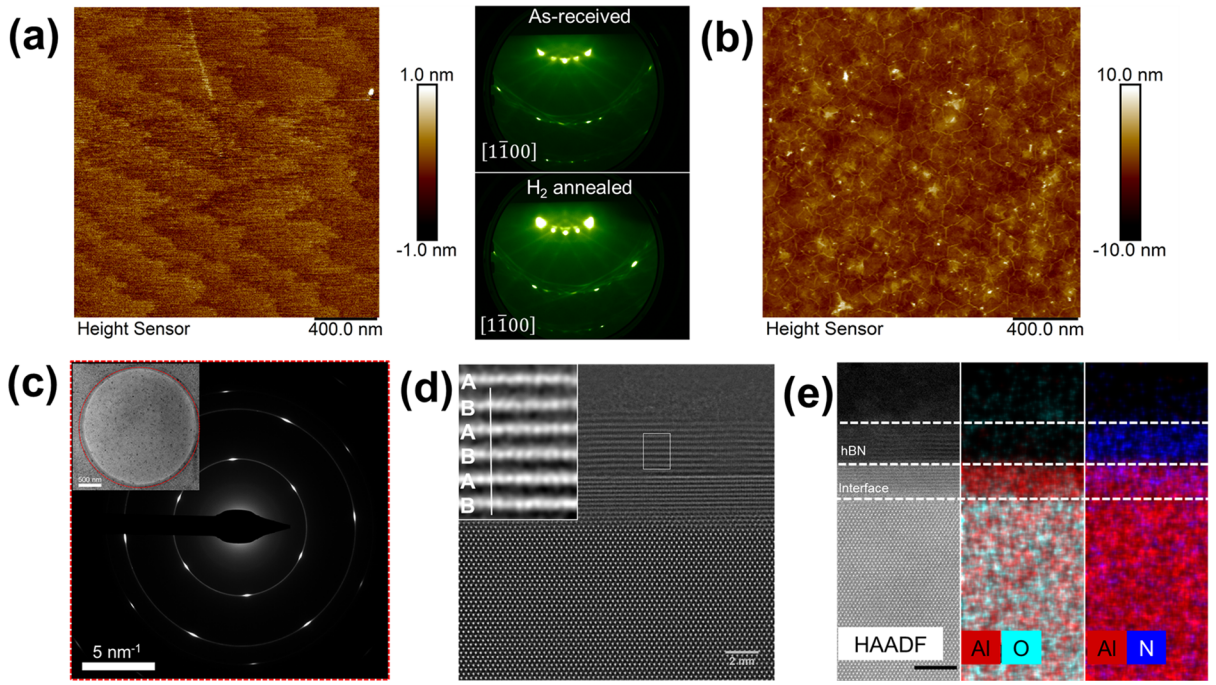

Figure 4. (a) AFM image of the H_2 annealed *A*-plane sapphire surface at 1300 °C. On the right side is the RHEED pattern of as-received *A*-plane sapphire and H_2 annealed *A*-plane sapphire indicating a negligible effect of H_2 annealing on the RHEED pattern of *A*-plane sapphire. (b) AFM image of the hBN deposited at 1300 °C (c) SAED pattern showing hBN films on sapphire with higher degree of polycrystallinity as indicated by rings between the bright spots collected from the circled area in the inset. The inset is a low magnification plan view TEM image showing a continuous film of BN with out-of-plane growth. (d) Cross-sectional HAADF-STEM micrograph of the sp^2-BN layers deposited on *A*-plane sapphire along zone axis [0001], with the rectangular region enlarged in the inset showing the hexagonal (ABAB...) stacking sequence of sp^2-BN. (e) HAADF-STEM image and corresponding EDS elemental maps indicating an interface composed of Al, O and N. Scale bar on the HAADF image is 5 nm.

process.[41] To approach the intrinsic properties of hBN, the film was transferred onto a SiO_2/Si substrate. Figure S1c,d shows 5 μm × 5 μm area maps of the peak position and FWHM, respectively, of the Raman E_{2g} peak of the hBN. The average peak position was 1365 ± 0.2 cm^{-1}, thus confirming sub-micrometer stress relaxation after film transfer. In addition, the average fwhm of the film was reduced to 18.5 ± 0.8 cm^{-1} which is the narrowest reported thus far for CVD grown hBN films.[23,25,37,38,42] The drop in standard deviation in the peak position and fwhm after film transfer as compared to as-grown hBN on sapphire shows the effect of inhomogeneous stress distribution in the as-grown hBN film which relaxes and homogenizes after film transfer to a Si/SiO_2 substrate. The Raman E_{2g} average fwhm of 18.5 cm^{-1} is higher compared to fwhm of ∼14.5 cm^{-1} of hBN obtained on metallic substrates using CVD indicating that there is further room for improvement in the quality of films obtained on non-metallic substrates.[43]

To investigate the onset of surface modification of the *C*-plane sapphire substrate and its impact on the growth and crystalline quality of hBN, 10 min H_2 annealing and further hBN deposition were carried out at lower growth temperatures (1150 °C and 1225 °C) compared to 1300 °C that was previously discussed. For the *C*-plane sapphire substrate annealed at 1150 °C, narrow terrace widths are observed similar to the as-received sapphire (Figure 3a) along with shallow pits that have begun to form, similar to prior reports on graphene growth at 1150 °C in a H_2 environment.[44] This suggest that at 1150 °C, the etching/transformation process has just begun which is further corroborated by the RHEED pattern obtained of the annealed substrate along the [1$\bar{1}$00] azimuth (Figure 3b). Besides the dominant diffraction pattern from the un-reconstructed sapphire surface of high intensity, very faint traces of the above discussed dense array of reconstruction diffractions are observed at the lower temperature anneal at 1150 °C. Those spots gain in intensity after the anneal at higher temperature (1225 °C) as seen in Figure 3b, which agrees with a more pronounced development of the surface reconstruction at higher temperature. This is further corroborated by the AFM image in Figure 3c of the H_2 annealed sapphire at 1225 °C. The terraces begin to widen with the annealing temperature indicating similar observations made for H_2 annealing at 1300 °C.

AFM images of hBN deposited at 1150 and 1225 °C (Figure S2a,b) show that the films are continuous with wrinkles similar to hBN growth at 1300 °C. (Figure S2c) confirms that the hBN film obtained on H_2 annealed sapphire substrate at 1150 and 1225 °C exhibits a certain degree of crystallographic order as indicated by the observed diffraction streaks with $[11\bar{2}0]_{hBN}$||$[1\bar{1}00]_{sapphire}$ epitaxial relation, however, the diffraction streaks are broad, diffuse and of low intensity indicating a high degree of disorder in the film as compared to the hBN obtained at the growth temperature of 1300 °C. This is further corroborated by Figure S2d which shows the Raman spectra of the hBN films obtained at different growth temperatures. The peak position for the Raman active E_{2g} mode is observed at 1368.5 cm^{-1}. Furthermore, the fwhm of the E_{2g} peak decreases as a function of temperature (32 cm^{-1} at 1150 °C, 27.2 cm^{-1} at 1225 °C and 24.5 cm^{-1} at 1300 °C) indicating that the hBN film quality improves as the growth temperature increases.

https://doi.org/10.1021/acsami.1c14591
ACS Appl. Mater. Interfaces 2021, 13, 54516−54526

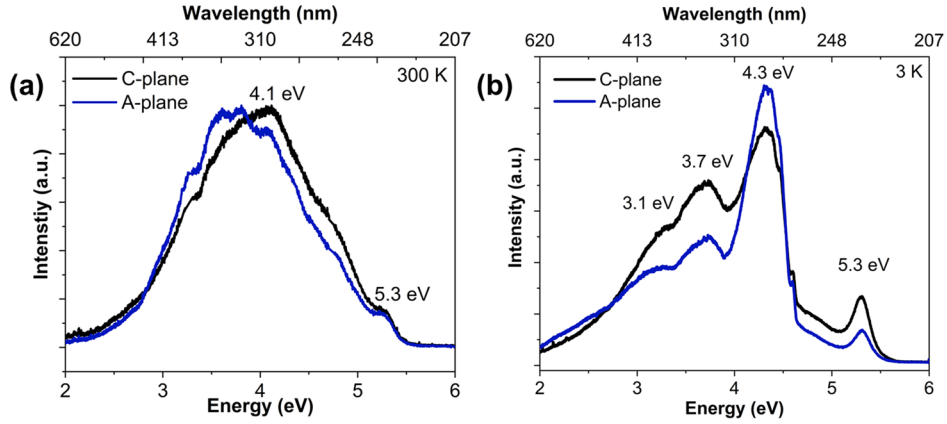

Figure 5. (a) RT PL of hBN as grown on *C* plane and *A* plane sapphire. The peak near 4.1 eV is attributed to a DAP transition between V_N; shallow donor, and C_N; deep acceptor. The peak near 5.3 eV is attributed to a quasi-DAP transition between V_N and an unknown deep acceptor (b) PL at 3 K of hBN grown on *C*-plane and *A*-plane sapphire. Peaks near 3.1, 3.7, 4.3, and 5.3 eV are resolved in the LT PL. Most probable origin of 3.1 eV is N_i due to its low formation energy. 3.7 eV peak is attributed to DAP radiative recombination. Origin of 4.3 eV peak is unknown, possible contribution from C and O. 5.3 eV peak is attributed to quasi-DAP transition.

From the results of hBN deposited on *C*-plane sapphire, it can be concluded that at the high temperatures required for depositing high crystalline quality hBN, the *C*-plane sapphire surface is unstable and undergoes significant modification which can directly impact the properties of the deposited hBN. For (opto)-electronic applications, there is a need for a smooth, flat and rigid insulating substrate. Therefore, hBN growth requires a crystalline inert template which is stable at high growth temperature. As an alternative, *A*-plane sapphire was investigated for hBN growth due to the higher stability of *A*-plane sapphire against loss of surface atoms due to smaller *d*-spacing between adjacent planes in case of *A*-plane compared to *C*-plane sapphire. The interplanar spacing (d) between the adjacent crystal planes of the sapphire is calculated to be 1.189 and 2.166 Å for *A*- and *C*-plane Al_2O_3 respectively.[45] Therefore, the energy required to remove material from the layer increases from *C*-plane to *A*-plane Al_2O_3. A similar annealing protocol to that previously discussed (i.e. 10 min H_2 annealing at 1300 °C) yielded minimal surface modification for *A*-plane sapphire. The surface roughness of the annealed *A*-plane sapphire is 0.3 nm (Figure 4a), almost half that of the H_2-annealed *C*-plane sapphire (0.5 nm). Furthermore, the RHEED pattern of the H_2-annealed surface is unchanged from that of the as-received surface (Figure 4a), in contrast to the case of *C*-plane sapphire substrate. Figure 4b shows an AFM image of the deposited hBN film on *A*-plane sapphire, showing a continuous film with higher wrinkle density as compared to hBN films grown on *C*-plane sapphire under identical growth conditions. This suggests a greater relaxation of residual stress in the film as compared to *C*-plane sapphire.

To assess the extent of residual stress in the deposited films, Raman mapping was performed over an area of 25 μm^2 (Figure S3). The average peak position of the E_{2g} mode of hBN on *A*-plane sapphire was found to be at 1366 ± 0.8 cm^{-1} with a FWHM of 24.5 ± 0.7 cm^{-1} which is in-between the value of 1365 cm^{-1} for fully relaxed hBN, and 1368.5 cm^{-1} measured for hBN on *C*-plane sapphire. This indicates that hBN on *A*-plane sapphire is under lower residual stress at RT compared to hBN on *C*-plane sapphire as observed using AFM as well. As discussed previously, the inhomogeneity in the film properties of hBN on *C*-plane sapphire is due to surface roughness and pits on the substrate surface. However, in case of *A*-plane sapphire, the surface appears smooth (Figure 4a). Thus, the Raman E_{2g} FWHM was measured over an area of 25 μm^2 to assess the inhomogeneity in the films (Figure S4). It is clear from the FWHM distribution that hBN deposited on *A*-plane sapphire has a lower standard deviation than that observed for *C*-plane sapphire as expected from the reduced surface roughness.

Figure 4c inset shows a low magnification plan view TEM image of the hBN film grown on *A*-plane sapphire and transferred onto a TEM grid. The transferred film is continuous but does contain out-of-plane growth where the hBN basal plane is not parallel to the basal plane of the substrate. This is evident from the small ring-like features present throughout in the inset figure. A high-resolution TEM image (Figure S5) obtained from one such feature confirms the out-of-plane oriented growth of the basal planes of hBN. These features are often referred to as inorganic fullerene structures in the literature.[46,47] The corresponding SAED pattern (Figure 4c) shows that the film is crystalline (six bright hexagonal spots) but also exhibits a higher degree of polycrystallinity (ring connecting the bright spots) which is likely due to the out-of-plane oriented fullerene structures.[46,47] Figure 4d is a high-resolution cross-sectional HAADF-STEM image acquired along the [0001] zone axis of the sapphire substrate to observe stacking sequence, and the interface between hBN and sapphire. As can be seen from the image, BN is layered, demonstrating the sp^2 nature of the hBN film on the substrate. A band pass filter was applied on the image to better visualize the atomic columns of layered sp^2-BN. Thus resolved atomic columns of sp^2-BN were used to identify the stacking sequence of the film. In the rectangular inset, a magnified image shows hexagonal (ABAB...) stacking of sp^2 BN. Figure 4e is a HAADF-STEM image of this sample showing hBN film on *A*-plane sapphire with a crystalline interface between hBN and sapphire. EDS reveals that the interface is composed mainly of Al, O, N. Unlike *C*-plane sapphire, Si is not observed in this case. The higher oxygen etching rate of *C*-plane sapphire compared to *A*-plane sapphire may lead to Si incorporation in case of *C*-plane sapphire which is not observed for *A*-plane sapphire.

PL spectroscopy measurements were used to assess and compare the optical properties of the hBN films grown on *C*-

https://doi.org/10.1021/acsami.1c14591
ACS Appl. Mater. Interfaces 2021, 13, 54516−54526

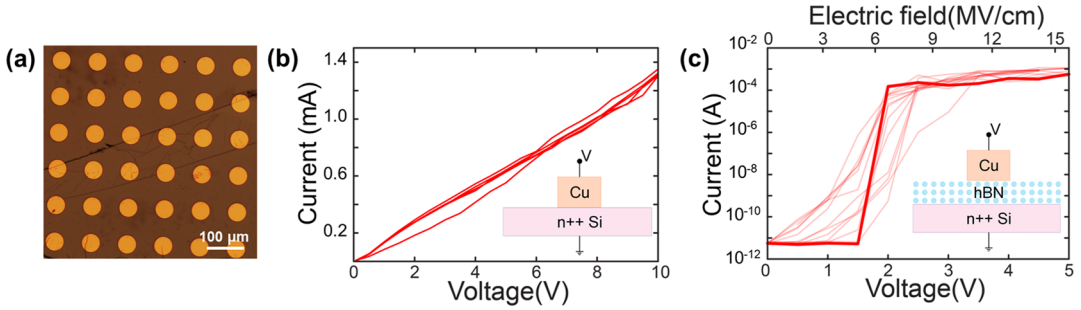

Figure 6. Dielectric properties of hBN transferred to n-Si substrates. (a) Optical image of the constructed capacitor-like structures with a diameter of 50 μm. Current−voltage characteristics of (b) Cu/n-Si and (c) Cu/hBN/n-Si where each curve corresponds to individual devices measured under an N_2 environment. Average breakdown voltage (electric field) of the devices equal to 1.5 V (5 MV cm^{-1}) and highlighted in red.

plane and *A*-plane sapphire. RT PL (Figure 5a) demonstrates that hBN grown on both orientations of sapphire have common luminescence characteristics with a peak near 4.1 eV, which has previously been attributed to a donor−acceptor pair (DAP) transition between a shallow donor and a deep acceptor, V_N and C_N respectively.[48] However, recent studies have attributed the 4.1 eV peak to a carbon dimer defect C_BC_N.[49] In addition, both samples have a peak near 5.3 eV, which has been identified as a quasi-DAP transition between V_N and an unknown deep acceptor. These are both signature peaks previously observed in hBN films grown using lower flow rates of NH_3.[48,50] The RT PL is resolved with a Gaussian peak fitting as shown in Figure S6 and an additional peak near 3.6 eV is identified possibly as a DAP radiative recombination at RT[51] and the FWHM of the overall defect peak is ∼1.4 eV. The PL at 3 K resolves the quasi-DAP peak (5.3 eV) as can be seen in Figure 5b. Additional peaks can also be resolved around 4.3, 3.7, and 3.1 eV at 3 K. The origin of the 4.3 eV peak is unclear; peaks near that energy has been correlated to the presence of carbon and oxygen impurities in the sample.[51,52] The 3.7 and 3.1 eV peaks have been seen previously by Museur et al. and Khorasani.[53,54] Museur and Kanaev identifies the 3.7 eV peak as a DAP radiative recombination.[53] Khorasani et al. has recently elucidated that the nitrogen interstitial (N_i) has the lowest formation energy and therefore provides the most favorable origin of the 3.1 eV peak.[54] An attempt was made to analyze the 3 K PL spectra by Gaussian peak fitting as well, however, it was difficult to unambiguously fit the overall spectra. Further studies are needed to understand the origins of the defect peaks with additional experiments or hybrid functional studies. According to both RT and LT (3 K) PL, hBN deposited on *C*-plane and *A*-plane sapphire do not show any significant differences in their optical properties.

To compare the dielectric breakdown characteristics of hBN obtained on *A*-plane sapphire with that of *C*-plane sapphire, several attempts were made to obtain large area hBN transferred from *C*-plane sapphire to n-doped Si, however, film transfer was unsuccessful, thus preventing a direct comparison of hBN dielectric breakdown field strength for films deposited on *C*-plane sapphire. The decoupling/detachment of hBN from the growth template appeared to be much easier when using *A*-plane sapphire rather than *C*-plane, which indicates a higher degree of vdW interaction between the as-grown hBN film on *C*-plane sapphire as compared to *A*-plane sapphire. During the wet transfer of 2D materials grown on sapphire, the two main mechanisms that contribute to the detachment of the 2D films from the growth substrate are: (i) the water and/or the Na ions intercalation at the interface and (2) chemical etching of the interface between the bulk and the 2D film. If there are pure vdW interactions between the 2D film and the substrate, intercalation of Na ions happens at a faster rate, especially since the NaOH makes the sapphire substrate hydrophilic. If there exist covalent bonds between the 2D film and the substrate, these may not get etched by NaOH and will pin the 2D film to the substrate. There likely exists some degree of covalent bonding between hBN on both *C*-plane and *A*-plane sapphire, but to a different extent, which can be inferred from the presence of wrinkles in the hBN film. If there exists weaker interaction between the film and the substrate, then the film can decouple from the substrate during cooldown resulting in wrinkles and greater relaxation of film stress. The *C*-plane sapphire also appears to be much more chemically reactive than *A*-plane sapphire under the hBN growth conditions, consequently, it is reasonable to expect more chemical bonds to form between hBN and *C*-plane sapphire compared to *A*-plane sapphire which is more inert. From the film transfer experiments that were performed during this study, it is understood that there is an interface which strongly bonds the hBN to the *C*-plane sapphire.

To evaluate the electrical properties of the hBN films on *A*-plane sapphire, the electrical breakdown strength was studied by measuring the output current as a function of applied voltage on vertically designed devices (Figure 6a). The hBN films were transferred from the growth substrates onto n-doped Si substrates followed by copper top electrode deposition resulting in a sandwich-type structure. A linear current−voltage dependence was observed in Cu/n-Si devices which are used as a reference (Figure 6b). For the Cu/hBN/n-Si devices, the leakage current sharply increases, and electrical breakdown of the devices occurs above 1.5 V on average (Figure 6c). The thickness of the film is around 3 nm which equals to 5 MV cm^{-1} breakdown field agreeing well with early reports on mechanically exfoliated hBN flakes.[55] Non-uniform current−voltage characteristics were observed from device-to-device which are most likely due to the wrinkles, cracks, and other line (point) defects that form during the wet transfer of the film.

3. CONCLUSIONS

This study investigated the effects of the CVD ambient and conditions on the surface of *C*-plane sapphire and its subsequent impact on hBN film growth and properties. At the high growth temperatures (∼1300 °C) required for hBN growth, oxygen desorbs from the Al_2O_3 surface leaving the surface Al rich. Continued etching of the *C*-plane sapphire

https://doi.org/10.1021/acsami.1c14591
ACS Appl. Mater. Interfaces 2021, 13, 54516−54526

surface in the high temperature H_2 environment results in a non-uniform surface morphology which translates into inhomogeneous residual stress in the hBN films. Thus, even though *C*-plane sapphire is a higher order symmetric plane with 6-fold symmetry, due to its instability under hBN growth conditions, it may not be the best choice for hBN deposition. *A*-plane sapphire was therefore investigated as an alternative substrate. Unlike *C*-plane, the *A*-plane sapphire surface does not modify under the growth conditions, thus proving to be a stable substrate for hBN deposition. hBN obtained on both the planes of sapphire were continuous with wrinkled morphology due to CTE mismatch with the substrate. Moreover, the films were rotationally oriented with respect to the substrate. In the case of BN obtained on *A*-plane sapphire, the stacking was identified to be ABAB, thus confirming the hexagonal phase of the film. To compare the quality of hBN obtained on *C*-plane and *A*-plane sapphire substrate, RT as well as 3 K PL measurements were performed. Using PL, nitrogen vacancies were identified in the hBN obtained on both orientations, with no considerable difference in the luminescence characteristics. Moreover, the calculated breakdown field strength of hBN obtained on *A*-plane sapphire is 5 MV cm^{-1} which agrees well with reports on mechanically exfoliated hBN flakes.

4. METHODS

4.1. hBN Growth Process. The growths were performed in a vertical, cold wall, inductively heated metalorganic CVD reactor, traditionally designed for group III-nitride growth such as GaN and AlN. The reactor design was modified to enable higher growth temperatures (up to ∼1500 °C) for hBN deposition.[56] B_2H_6 (0.2% in H_2) and NH_3 were used as precursors for B and N, respectively using H_2 as a carrier gas. B_2H_6 reacts with NH_3 at temperatures as low as RT to form $H_3N{-}BH_3$ and other volatile B−N species, consequently, gas phase reactions can impact the deposition process to a great extent. Therefore, the growths were performed using pulsed growth mode more commonly known as FME method to suppress the parasitic gas phase reactions between the precursors. α-Al_2O_3 wafers, purchased from Cryscore Optoelectronic Limited, were used for hBN deposition. Growths were performed on two different planes of substrates: on axis *C*-plane (0001) and on axis *A*-plane $(11\bar{2}0)$ with ±0.2° miscut. Prior to hBN deposition, the substrates were diced to 1 × 1 cm^2 size and cleaned using standard cleaning procedure to remove organic residues. It includes 10 min ultra-sonication in acetone followed by isopropyl alcohol and rinsing in DI water for at least 10 times. Lastly, substrates were dipped in Piranha solution [mixture of sulfuric acid (H_2SO_4), water, and hydrogen peroxide (H_2O_2)] at 140 °C for 40 min to remove any organic residues from the surface. Substrates were then annealed in hydrogen ambient at 1300 °C for 10 min to remove remaining organic residues, polishing marks, resulting in a clean surface with atomic terraces. The growths were performed at a temperature of 1300 °C and at a pressure of 50 Torr. V/III ratio used for the growths was 4000. In the FME scheme, 0.05 sccm of B_2H_6 along with 200 sccm of NH_3 were fed into the reactor alternatively along with a total H_2 flow rate of 7.5 slm. Pulse time for B_2H_6 and NH_3 was 2 and 1 s, respectively. The growth schematic is shown in Supporting Information (Figure S7). Number of pulses were varied to precisely control the hBN thickness.

4.2. Atomic Force Microscopy. AFM was performed to analyze surface morphology using a Bruker Dimension Icon AFM system. OLTESPA-R3 air probe AFM tips with a nominal tip radius of ∼7 nm and spring constant of 2 N/m were employed for the measurements. Images were collected using peak-force tapping mode.

4.3. Raman Spectroscopy. Raman spectra was collected by using a HORIBA LabRAM HR Evolution high spectral resolution analytical Raman microscope "Lucy" with a laser wavelength of 488 nm and laser power of 5 mW.

4.4. FTIR Spectroscopy. FTIR measurements were performed on a vertex 70 spectrometer (Bruker Opitcs, Bellerica MA) equipped with a liquid nitrogen cooled narrow band mercury cadmium telluride detector. IR spectra were acquired in specular reflection geometry using a Veemax variable angle accessory (pike tech, cottonwood WI) at an incident angle of 30°. A total of 100 scans were averaged at 6 cm^{-1} resolution per spectrum and reflectance calculated by referencing to bare sapphire.

4.5. Reflection High Energy Electron Diffraction. For RHEED analysis, samples were transferred into an adjacent model R450 molecular beam epitaxy (MBE) system from DCA Instruments. The time that samples dedicated for RHEED studies stayed in ambient conditions was kept as short as possible to minimize surface contamination. RHEED images were collected using a STAIB instruments electron gun with an energy of 15 keV and a filament current of 1.45 A at a background pressure in the MBE chamber of 5 × 10^{-10} Torr. The sample was heated to 120 °C for 30 min in the load lock chamber to remove any water vapor from the surface. The projected RHEED patterns were collected with a kSA 400 RHEED camera and software package.

4.6. PL Spectroscopy. PL spectroscopy was conducted at RT using an ArF laser with a 193 nm wavelength and an excitation power density of <1 kW/cm^2. The luminescence from the sample was directed onto a 0.75-m focal length Acton Series SP-2750 monochromator. 150 grooves/mm diffraction grating was used as a dispersive element. Princeton Instruments (SP2750 0.75 m) spectrometer with an attached PIXIS 2 K charge-coupled device camera recorded the PL spectra.

4.7. Cross-Sectional TEM. Cross-sectional TEM specimens were prepared on a FEI Helios 660 focused ion beam (FIB) system. 1 kV final cleaning was applied after samples became electron transparent to avoid ion beam damage to the sample surfaces. Atomic resolution HAADF-STEM imaging was performed on a Thermo Fisher aberration corrected S/TEM at 300 kV (Titan^3 G2 60-300). Energy-dispersive X-ray spectroscopic (EDS) elemental maps were collected using a SuperX EDS system (Bruker) under STEM mode.

4.8. PMMA Based Transfer Process. The hBN deposited on sapphire was transferred onto desired substrates (90 nm thick SiO_2/Si for Raman measurements, n-Si for dielectric breakdown measurements, Cu TEM grid for plan view TEM) using a wet poly(methyl methacrylate) (PMMA)-assisted approach with slight modifications depending on the target substrate. During a typical process, PMMA was first spin-coated (PMMA 6% 950A, 2000 rpm) directly on the hBN surface and cured at 100 °C for 10 min to improve PMMA/hBN adhesion. To facilitate the sapphire etching and ion intercalation at the hBN-sapphire interface, PMMA was scratched away from the sample edges. The sample was then immersed into a NaOH solution (1 M) at 70 °C until the PMMA/hBN fully detaches from the sapphire and floats on the surface. The PMMA/hBN film was then thoroughly rinsed using DI water and scooped with the target substrate. After drying overnight at RT, the sample was annealed at about 110−120 °C for 5 min to improve the contact between hBN and the target substrate. Finally, the PMMA was removed using acetone and the sample was rinsed using IPA before being dried with a N_2 gun.

4.9. Plan View TEM. Plan view TEM specimens of as-grown hBN films were prepared using the wet PMMA-assisted transfer method detailed in the previous section, the target substrate being a Quantifoil Cu TEM grid. Imaging and SAED studies were performed on thus prepared specimens using a F200X scanning/TEM operated at 80 kV.

4.10. Device Fabrication and Dielectric Breakdown Measurements. The transferred hBN films were patterned using the Raith EBPG-5200 e-beam lithography tool. 120 nm thick Cu electrodes were deposited using Temescal e-beam evaporator where the diameter of each individual device was 50 μm. The current−voltage characteristics of the films in Cu/hBN/n-Si and Cu/n-Si stacks were measured using a FormFactor 11000 semi-automatic probe station in N_2 environment.

https://doi.org/10.1021/acsami.1c14591
ACS Appl. Mater. Interfaces 2021, 13, 54516−54526

■ ASSOCIATED CONTENT

Supporting Information

The Supporting Information is available free of charge at https://pubs.acs.org/doi/10.1021/acsami.1c14591.

Raman spectroscopy before and after hBN film transfer from *C*-plane sapphire, film characterization of hBN deposited at different temperatures, Raman spectroscopy of hBN deposited on *C*-plane and *A*-plane sapphire, plan view TEM of hBN deposited on *A*-plane sapphire (PDF)

■ AUTHOR INFORMATION

Corresponding Author

Joan M. Redwing − *Department of Materials Science and Engineering, The Pennsylvania State University, University Park, Pennsylvania 16802, United States; 2D Crystal Consortium—Materials Innovation Platform, The Pennsylvania State University, University Park, Pennsylvania 16802, United States;* orcid.org/0000-0002-7906-452X; Email: jmr31@psu.edu

Authors

Anushka Bansal − *Department of Materials Science and Engineering, The Pennsylvania State University, University Park, Pennsylvania 16802, United States;* orcid.org/0000-0003-4340-362X

Maria Hilse − *2D Crystal Consortium—Materials Innovation Platform, The Pennsylvania State University, University Park, Pennsylvania 16802, United States*

Benjamin Huet − *2D Crystal Consortium—Materials Innovation Platform, The Pennsylvania State University, University Park, Pennsylvania 16802, United States;* orcid.org/0000-0003-4084-5705

Ke Wang − *Materials Research Institute, The Pennsylvania State University, University Park, Pennsylvania 16802, United States*

Azimkhan Kozhakhmetov − *Department of Materials Science and Engineering, The Pennsylvania State University, University Park, Pennsylvania 16802, United States*

Ji Hyun Kim − *Department of Materials Science and Engineering, North Carolina State University, Raleigh, North Carolina 27695, United States*

Saiphaneendra Bachu − *Department of Materials Science and Engineering, The Pennsylvania State University, University Park, Pennsylvania 16802, United States;* orcid.org/0000-0001-9898-7349

Nasim Alem − *Department of Materials Science and Engineering, The Pennsylvania State University, University Park, Pennsylvania 16802, United States; 2D Crystal Consortium—Materials Innovation Platform, The Pennsylvania State University, University Park, Pennsylvania 16802, United States;* orcid.org/0000-0003-0009-349X

Ramon Collazo − *Department of Materials Science and Engineering, North Carolina State University, Raleigh, North Carolina 27695, United States*

Joshua A. Robinson − *Department of Materials Science and Engineering, The Pennsylvania State University, University Park, Pennsylvania 16802, United States; 2D Crystal Consortium—Materials Innovation Platform, The Pennsylvania State University, University Park, Pennsylvania 16802, United States*

Roman Engel-Herbert − *Department of Materials Science and Engineering, The Pennsylvania State University, University Park, Pennsylvania 16802, United States; 2D Crystal Consortium—Materials Innovation Platform, The Pennsylvania State University, University Park, Pennsylvania 16802, United States*

Complete contact information is available at: https://pubs.acs.org/10.1021/acsami.1c14591

Author Contributions

The manuscript was written through contributions of all authors. All authors have given approval to the final version of the manuscript.

Notes

The authors declare no competing financial interest.

■ ACKNOWLEDGMENTS

Financial support was provided by the National Science Foundation through the 2D Crystal Consortium—Materials Innovation Platform (2DCC-MIP) at The Pennsylvania State University under NSF cooperative agreement DMR-1539916 and ECCS-2029729. S.B. and N.A. also acknowledge NSF CAREER DMR-1654107. A.K. and J.A.R. acknowledge Intel through the Semiconductor Research Corporation (SRC) Task 2746. R.C. and J.H.K. acknowledge funding in part from NSF (ECCS-1653383). We thank Haiying Wang for TEM sample preparation using FIB. All microscopy work was performed at the Penn State Materials Characterization Laboratory.

■ REFERENCES

(1) Caldwell, J. D.; Aharonovich, I.; Cassabois, G.; Edgar, J. H.; Gil, B.; Basov, D. N. Photonics with Hexagonal Boron Nitride. *Nat. Rev. Mater.* **2019**, *4*, 552−567.

(2) Sajid, A.; Ford, M. J.; Reimers, J. R. Single-Photon Emitters in Hexagonal Boron Nitride: A Review of Progress. *Rep. Prog. Phys.* **2020**, *83*, 044501.

(3) Meng, J.; Wang, D.; Cheng, L.; Gao, M. Recent Progress in Synthesis , Properties , and Applications of Hexagonal Boron Nitride-Based Heterostructures. *Nanotechnology* **2019**, *30*, 74003.

(4) Cho, Y.-J.; Summerfield, A.; Davies, A.; Cheng, T. S.; Smith, E. F.; Mellor, C. J.; Khlobystov, A. N.; Foxon, C. T.; Eaves, L.; Beton, P. H.; Novikov, S. V. Hexagonal Boron Nitride Tunnel Barriers Grown on Graphite by High Temperature Molecular Beam Epitaxy. *Sci. Rep.* **2016**, *6*, 34474.

(5) Rigosi, A. F.; Hill, H. M.; Glavin, N. R.; Pookpanratana, S. J.; Yang, Y. Measuring the Dielectric and Optical Response of Millimeter-Scale Amorphous and Hexagonal Boron Nitride Films Grown on Epitaxial Graphene Measuring the Dielectric and Optical Response of Millimeter-Scale Amorphous and Hexagonal Boron Nitride Films Grown O. *2D Mater.* **2018**, *5*, 011011.

(6) Koperski, M.; Vaclavkova, D.; Watanabe, K.; Taniguchi, T.; Novoselov, K. S.; Potemski, M. Midgap Radiative Centers in Carbon-Enriched Hexagonal Boron Nitride. *Proc. Natl. Acad. Sci. U.S.A.* **2020**, *117*, 13214.

(7) Tran, T. T.; Bray, K.; Ford, M. J.; Toth, M.; Aharonovich, I. Quantum Emission from Hexagonal Boron Nitride Monolayers. *Nat. Nanotechnol.* **2016**, *11*, 37−41.

(8) Jiang, H. X.; Lin, J. Y. Review—Hexagonal Boron Nitride Epilayers: Growth, Optical Properties and Device Applications. *ECS J. Solid State Sci. Technol.* **2017**, *6*, Q3012−Q3021.

(9) Jungwirth, N. R.; Calderon, B.; Ji, Y.; Spencer, M. G.; Flatté, M. E.; Fuchs, G. D. Temperature Dependence of Wavelength Selectable Zero-Phonon Emission from Single Defects in Hexagonal Boron Nitride. *Nano Lett.* **2016**, *16*, 6052−6057.

(10) Schué, L.; Berini, B.; Betz, A. C.; Plaçais, B.; Ducastelle, F.; Barjon, J.; Loiseau, A. Dimensionality Effects on the Luminescence Properties of HBN. *Nanoscale* **2016**, *8*, 6986−6993.
(11) Zhang, X.; Zhang, F.; Wang, Y.; Schulman, D. S.; Zhang, T.; Bansal, A.; Alem, N.; Das, S.; Crespi, V. H.; Terrones, M.; Redwing, J. M. Defect-Controlled Nucleation and Orientation of WSe2 on HBN: A Route to Single-Crystal Epitaxial Monolayers. *ACS Nano* **2019**, *13*, 3341−3352.
(12) Liu, Z.; Ma, L.; Shi, G.; Zhou, W.; Gong, Y.; Lei, S.; Yang, X.; Zhang, J.; Yu, J.; Hackenberg, K. P.; Babakhani, A.; Idrobo, J.-C.; Vajtai, R.; Lou, J.; Ajayan, P. M. In-Plane Heterostructures of Graphene and Hexagonal Boron Nitride with Controlled Domain Sizes. *Nat. Nanotechnol.* **2013**, *8*, 119.
(13) Kim, K. K.; Lee, H. S.; Lee, Y. H. Synthesis of Hexagonal Boron Nitride Heterostructures for 2D van Der Waals Electronics. *Chem. Soc. Rev.* **2018**, *47*, 6342−6369.
(14) Shi, Y.; Hamsen, C.; Jia, X.; Kim, K. K.; Reina, A.; Hofmann, M.; Hsu, A. L.; Zhang, K.; Li, H.; Juang, Z.-Y.; Dresselhaus, M. S.; Li, L.-J.; Kong, J. Synthesis of Few-Layer Hexagonal Boron Nitride Thin Film by Chemical Vapor Deposition. *Nano Lett.* **2010**, *10*, 4134−4139.
(15) Ismach, A.; Chou, H.; Ferrer, D. A.; Wu, Y.; McDonnell, S.; Floresca, H. C.; Covacevich, A.; Pope, C.; Piner, R.; Kim, M. J.; Wallace, R. M.; Colombo, L.; Ruoff, R. S. Toward the Controlled Synthesis of Hexagonal Boron Nitride Films. *ACS Nano* **2012**, *6*, 6378−6385.
(16) Caneva, S.; Weatherup, R. S.; Bayer, B. C.; Blume, R.; Cabrero-Vilatela, A.; Braeuninger-Weimer, P.; Martin, M.-B.; Wang, R.; Baehtz, C.; Schloegl, R.; Meyer, J. C.; Hofmann, S. Controlling Catalyst Bulk Reservoir Effects for Monolayer Hexagonal Boron Nitride CVD. *Nano Lett.* **2016**, *16*, 1250−1261.
(17) Nakamura, K. Preparation and Properties of Boron Nitride Films by Metal Organic Chemical Vapor Deposition. *J. Electrochem. Soc.* **1986**, *133*, 1120−1123.
(18) Chubarov, M.; Pedersen, H.; Högberg, H.; Henry, A. On the Effect of Silicon in CVD of Sp2 Hybridized Boron Nitride Thin Films. *CrystEngComm* **2013**, *15*, 455−458.
(19) Chubarov, M.; Pedersen, H.; Högberg, H.; Czigány, Z.; Garbrecht, M.; Henry, A. Polytype Pure Sp2-BN Thin Films As Dictated by the Substrate Crystal Structure. *Chem. Mater.* **2015**, *27*, 1640−1645.
(20) Chubarov, M.; Pedersen, H.; Högberg, H.; Henry, A.; Czigány, Z. Initial Stages of Growth and the Influence of Temperature during Chemical Vapor Deposition of Sp 2 -BN Films. *J. Vac. Sci. Technol., A* **2015**, *33*, 061520.
(21) Kobayashi, Y.; Hibino, H.; Nakamura, T.; Akasaka, T.; Makimoto, T.; Matsumoto, N. Boron Nitride Thin Films Grown on Graphitized 6H-SiC Substrates by Metalorganic Vapor Phase Epitaxy. *Jpn. J. Appl. Phys.* **2007**, *46*, 2554−2557.
(22) Yamada, H.; Inotsume, S.; Kumagai, N.; Yamada, T.; Shimizu, M. Comparative Study of Boron Precursors for Chemical Vapor-Phase Deposition-Grown Hexagonal Boron Nitride Thin Films. *Phys. Status Solidi A* **2021**, *218*, 2000241.
(23) Li, X.; Sundaram, S.; El Gmili, Y.; Ayari, T.; Puybaret, R.; Patriarche, G.; Voss, P. L.; Salvestrini, J. P.; Ougazzaden, A. Large-Area Two-Dimensional Layered Hexagonal Boron Nitride Grown on Sapphire by Metalorganic Vapor Phase Epitaxy. *Cryst. Growth Des.* **2016**, *16*, 3409−3415.
(24) Mendelson, N.; Chugh, D.; Reimers, J. R.; Cheng, T. S.; Gottscholl, A.; Long, H.; Mellor, C. J.; Zettl, A.; Dyakonov, V.; Beton, P. H.; Novikov, S. V.; Jagadish, C.; Tan, H. H.; Ford, M. J.; Toth, M.; Bradac, C.; Aharonovich, I. Identifying Carbon as the Source of Visible Single-Photon Emission from Hexagonal Boron Nitride. *Nat. Mater.* **2020**, *20*, 321−328.
(25) Chugh, D.; Wong-Leung, J.; Li, L.; Lysevych, M.; Tan, H. H.; Jagadish, C. Flow Modulation Epitaxy of Hexagonal Boron Nitride. *2D Mater.* **2018**, *5*, 045018.
(26) Ahmed, K.; Dahal, R.; Weltz, A.; Lu, J. J.-Q.; Danon, Y.; Bhat, I. B. Effects of Sapphire Nitridation and Growth Temperature on the Epitaxial Growth of Hexagonal Boron Nitride on Sapphire. *Mater. Res. Express* **2017**, *4*, 015007.
(27) Ueda, Y.; Yamada, J.; Ono, T.; Maruyama, T.; Naritsuka, S. Crystal Orientation Effects of Sapphire Substrate on Graphene Direct Growth by Metal Catalyst-Free Low-Pressure CVD. *Appl. Phys. Lett.* **2019**, *115*, 013103.
(28) Saito, K.; Ogino, T. Direct Growth of Graphene Films on Sapphire (0001) and (1120) Surfaces by Self-Catalytic Chemical Vapor Deposition. *J. Phys. Chem. C* **2014**, *118*, 5523−5529.
(29) Mishra, N.; Forti, S.; Fabbri, F.; Martini, L.; McAleese, C.; Conran, B. R.; Whelan, P. R.; Shivayogimath, A.; Jessen, B. S.; Buß, L.; Falta, J.; Aliaj, I.; Roddaro, S.; Flege, J. I.; Bøggild, P.; Teo, K. B. K.; Coletti, C. Wafer-Scale Synthesis of Graphene on Sapphire: Toward Fab-Compatible Graphene. *Small* **2019**, *15*, 1904906.
(30) Page, R.; Casamento, J.; Cho, Y.; Rouvimov, S.; Xing, H. G.; Jena, D. Rotationally Aligned Hexagonal Boron Nitride on Sapphire by Higherature Molecular Beam Epitaxy. *Phys. Rev. Mater.* **2019**, *3*, 064001.
(31) Ahn, J.; Rabalais, J. W. Composition and Structure of the Al2O3{0001}-(1 × 1) Surface. *Surf. Sci.* **1997**, *388*, 121−131.
(32) Gautier, M.; Fenaud, G.; Pham Van, L.; Villette, B.; Pollak, M.; Thromat, N.; Jollet, F.; Duraud, J.-P. Alpha-Al2O3 (0001) Surfaces: Atomic and Electronic Structure. *J. Am. Ceram. Soc.* **1994**, *77*, 323−334.
(33) Jarvis, E. A. A.; Carter, E. A. Metallic Character of the Al 2 O 3 (0001)-($\sqrt{31} \times \sqrt{31}$) R ± 9° Surface Reconstruction. *J. Phys. Chem. B* **2001**, *105*, 4045−4052.
(34) El Sayah, Z.; Brahmi, R.; Beauchet, R.; Batonneau, Y.; Kappenstein, C. Synthesis, Characterization and Treatment of Alane (Aluminium Hydride, AlH3). *7th European Conference for Aeronautics and Space Sciences*, 2017; Vol. *1−14*.
(35) Turley, J. W.; Rinn, H. W. Crystal Structure of Aluminum Hydride. *Inorg. Chem.* **1969**, *8*, 18−22.
(36) Vangala, S.; Siegel, G.; Prusnick, T.; Snure, M. Wafer Scale BN on Sapphire Substrates for Improved Graphene Transport. *Sci. Rep.* **2018**, *8*, 8842.
(37) Snure, M.; Paduano, Q.; Kiefer, A. Effect of Surface Nitridation on the Epitaxial Growth of Few-Layer Sp2 BN. *J. Cryst. Growth* **2016**, *436*, 16−22.
(38) Paduano, Q.; Snure, M.; Weyburne, D.; Kiefer, A.; Siegel, G.; Hu, J. Metalorganic Chemical Vapor Deposition of Few-Layer Sp2 Bonded Boron Nitride Films. *J. Cryst. Growth* **2016**, *449*, 148−155.
(39) Gorbachev, R. V.; Riaz, I.; Nair, R. R.; Jalil, R.; Britnell, L.; Belle, B. D.; Hill, E. W.; Novoselov, K. S.; Watanabe, K.; Taniguchi, T.; Geim, A. K.; Blake, P. Hunting for Monolayer Boron Nitride: Optical and Raman Signatures. *Small* **2011**, *7*, 465−468.
(40) Kubota, Y.; Watanabe, K.; Tsuda, O.; Taniguchi, T. Deep Ultraviolet Light-Emitting Hexagonal Boron Nitride Synthesized at Atmospheric Pressure. *Science* **2007**, *317*, 932−934.
(41) Huet, B.; Raskin, J.-P.; Snyder, D. W.; Redwing, J. M. Fundamental Limitations in Transferred CVD Graphene Caused by Cu Catalyst Surface Morphology. *Carbon* **2020**, *163*, 95−104.
(42) Chugh, D.; Jagadish, C.; Tan, H. Large-Area Hexagonal Boron Nitride for Surface Enhanced Raman Spectroscopy. *Adv. Mater. Technol.* **2019**, *4*, 1900220.
(43) Chen, T.-A.; Chuu, C.-P.; Tseng, C.-C.; Wen, C.-K.; Wong, H.-S. P.; Pan, S.; Li, R.; Chao, T.-A.; Chueh, W.-C.; Zhang, Y.; Fu, Q.; Yakobson, B. I.; Chang, W.-H.; Li, L.-J. Wafer-Scale Single-Crystal Hexagonal Boron Nitride Monolayers on Cu (111). *Nature* **2020**, *579*, 219−223.
(44) Saito, K.; Ogino, T. Direct Growth of Graphene Films on Sapphire (0001) and (1120) Surfaces by Self-Catalytic Chemical Vapor Deposition. *J. Phys. Chem. C* **2014**, *118*, 5523−5529.
(45) Cao, L.; Zhang, X.; Yuan, J.; Guo, L.; Hong, T.; Hang, W.; Ma, Y. Study on the Influence of Sapphire Crystal Orientation on Its Chemical Mechanical Polishing. *Appl. Sci.* **2020**, *10*, 8065.
(46) Cain, J. D.; Shi, F.; Wu, J.; Dravid, V. P. Growth Mechanism of Transition Metal Dichalcogenide Monolayers: The Role of Self-Seeding Fullerene Nuclei. *ACS Nano* **2016**, *10*, 5440−5445.

https://doi.org/10.1021/acsami.1c14591
ACS Appl. Mater. Interfaces 2021, 13, 54516−54526

(47) Li, X. L.; Li, Y. D. Formation of MoS2 Inorganic Fullerenes (IFs) by the Reaction of MoO3 Nanobelts and S. *Chem.—Eur. J.* **2003**, *9*, 2726−2731.
(48) Du, X. Z.; Li, J.; Lin, J. Y.; Jiang, H. X. The Origin of Deep-Level Impurity Transitions in Hexagonal Boron Nitride. *Appl. Phys. Lett.* **2015**, *106*, 021110.
(49) Mackoit-Sinkevičienė, M.; Maciaszek, M.; Van de Walle, C. G.; Alkauskas, A. Carbon Dimer Defect as a Source of the 4.1 EV Luminescence in Hexagonal Boron Nitride. *Appl. Phys. Lett.* **2019**, *115*, 212101.
(50) Du, X. Z.; Li, J.; Lin, J. Y.; Jiang, H. X. The Origins of near Band-Edge Transitions in Hexagonal Boron Nitride Epilayers. *Appl. Phys. Lett.* **2016**, *108*, 052106.
(51) Zunger, A.; Katzir, A. Point Defects in Hexagonal Boron Nitride. II. Theoretical Studies. *Phys. Rev. B: Solid State* **1975**, *11*, 2378.
(52) Museur, L.; Anglos, D.; Petitet, J.-P.; Michel, J.-P.; Kanaev, A. V. Photoluminescence of Hexagonal Boron Nitride: Effect of Surface Oxidation under UV-Laser Irradiation. *J. Lumin.* **2007**, *127*, 595−600.
(53) Museur, L.; Kanaev, A. Photoluminescence Properties of Pyrolytic Boron Nitride. *J. Mater. Sci.* **2009**, *44*, 2560−2565.
(54) Khorasani, E.; Frauenheim, T.; Aradi, B.; Deák, P. Identification of the Nitrogen Interstitial as Origin of the 3.1 EV Photoluminescence Band in Hexagonal Boron Nitride. *Phys. Status Solidi A* **2021**, *258*, 2100031.
(55) Hong, S.; Lee, C.-S.; Lee, M.-H.; Lee, Y.; Ma, K. Y.; Kim, G.; Yoon, S. I.; Ihm, K.; Kim, K.-J.; Shin, T. J.; Kim, S. W.; Jeon, E.-c.; Jeon, H.; Kim, J.-Y.; Lee, H.-I.; Lee, Z.; Antidormi, A.; Roche, S.; Chhowalla, M.; Shin, H.-J.; Shin, H. S. Ultralow-Dielectric-Constant Amorphous Boron Nitride. *Nature* **2020**, *582*, 511−514.
(56) Bansal, A.; Zhang, X.; Redwing, J. Gas Source Chemical Vapor Deposition of Hexagonal Boron Nitride on C-Plane Sapphire. *J. Mater. Res.* **2021**.

https://doi.org/10.1021/acsami.1c14591
ACS Appl. Mater. Interfaces 2021, 13, 54516−54526